scientific reports

Check for updates

OPEN

Analysis of Rayleigh wave dynamic response and propagation characteristics in layered site

Hao Lv[1,2]✉

Rayleigh waves are crucial in earthquake engineering due to their significant contribution to structural damage. This study aims to accurately synthesize Rayleigh wave fields in both uniform elastic half-spaces and horizontally layered elastic half-spaces. To achieve this, we developed a self-programmed FORTRAN program utilizing the thin layer stiffness matrix method. The accuracy of the synthesized wave fields was validated through numerical examples, demonstrating the program's reliability for both homogeneous and layered half-space scenarios. A comprehensive analysis of Rayleigh wave propagation characteristics was conducted, including elliptical particle motion, depth-dependent decay, and energy concentration near the surface. The computational efficiency of the self-programmed FORTRAN program was also verified. This research contributes to a deeper understanding of Rayleigh wave behavior and lays the foundation for further studies on soil-structure interaction under Rayleigh wave excitation, ultimately improving the safety and resilience of structures in seismic-prone regions.

Keywords Rayleigh waves, Synthesize, Uniform elastic half-space, FORTRAN program, Site effects

Rayleigh-wave, which is the result of interfering P- and SV-waves at the free surface and travels along the free surface, is highly regarded in seismology fields, especially in near-surface geophysical exploration[1–3]. First identified by Rayleigh in 1885, these waves have been a subject of extensive study due to their slow decay along the surface and their predominance in seismic wave fields, carrying approximately two-thirds of the total seismic energy[4,5]. The characteristics of Rayleigh waves, such as their velocity variation and the phenomenon of dispersion, have been investigated thoroughly, leading to the development of various methods for calculating dispersion curves, which describe the relationship between phase velocity and frequency for different wave modes[6]. Rayleigh waves have been extensively observed in seismic exploration and play an important role in near-surface geophysical exploration, e.g., widely used in urban underground space exploration[7–9], subsurface parameter inversion[10,11] and layer thickness identification[12–14]. Therefore, the accurate simulation of Rayleigh waves is crucial in comprehending the mechanism of seismic-wave propagation and constructing reliable subsurface models.

The influences of anisotropy and viscoelasticity on Rayleigh waves were more intricate than their effects on body waves, owing to the stringent generation criteria for Rayleigh waves. This complexity has drawn the attention of numerous researchers, who have investigated Rayleigh wave behavior in anisotropic or viscoelastic media from various perspectives[15]. To this end, multiple studies have endeavored to examine the diffraction of Rayleigh waves around alluvial valleys, utilizing both analytical and numerical approaches. Certain researchers have estimated the near-surface quality factors through constrained inversion of attenuation coefficients derived from the amplitude data of viscoelastic Rayleigh waves[16]. Carcione[17] analyzed the propagation characteristic of viscoelastic Rayleigh-wave by pseudospectral modeling in time–space (t–x) domain, and results present the substantial differences compared with the pure elastic cases. In accordance with the work of Carcione, Zhang et al.[18] modeled the viscoelastic Rayleigh-wave via pseudospectral method and analyzed the phase velocity dispersion of Rayleigh-wave. The analytical method of Rayleigh waves is often referred to as the wave function expansion method[19], and the numerical methods include the finite element method[20], finite difference method[21], boundary element method[22], discrete wave number method[23], hybrid method[24], etc. Several researchers have theoretically examined the characteristics of viscoelastic Rayleigh waves from an energy perspective, noting that phase velocities and attenuation factors provide a reliable approximation of the wave's dispersion and dissipation[25,26]. However, some studies have conducted numerical modeling of viscoelastic Rayleigh wave fields,

[1]College of Safety and Environmental Engineering, Shandong University of Science and Technology, Qingdao 266590, China. [2]Department of Civil and Airport Engineering, Nanjing University of Aeronautics and Astronautics, Nanjing 20016, China. ✉email: lvhao_happy@sina.com

with the results indicating substantial differences from the pure elastic cases[18]. To gain a more comprehensive understanding of Rayleigh wave phenomena in Earth's media, it is essential to investigate their characteristics through numerical modeling.

In horizontally layered media, Rayleigh waves propagate in distinct modes with varying phase velocities, and their accurate synthesis is crucial for understanding soil-structure interactions (SSI) under seismic excitation. In the layered media where the layer stiffness increases with the depth of layers, the surface vibration was dominated by the fundamental mode of Rayleigh waves. Soil properties play important roles in advanced soil modeling, dynamic analysis of the SSIs and numerical simulations. The free-surface boundary condition severely affects the accuracy of Rayleigh-waves simulation[27]. In related theoretical studies, the vacuum formalism is an early and efficient scheme that simulates Rayleigh waves by setting the S-wave-related parameters to zero. Nevertheless, this method suffers from severe numerical dispersion due to the inability to use high-order spatial difference operators[28], thus not being able to achieve the accuracy requirements of surface-wave simulation[29]. The stress image method is a more suitable option because of its stability and accuracy[30,31], but it lacks rigorous mathematical proof. Generally, Rayleigh waves suffer more severe numerical dispersion than body waves owing to energy leaking into the domain above the free surface or the low-velocity structure. To achieve similar simulation accuracies between Rayleigh and body waves, small time or space steps may be adopted, resulting in a significant increase in computational requirements[32,33]. Earth materials usually behave as an imperfectly elastic medium[34], affecting the characteristics of Rayleigh waves in terms of amplitude and phase during their propagation[35]. Yuan et al.[36] analyzed the attenuation and dispersion of Rayleigh waves by comparing elastic and viscoelastic wavefields. The abovementioned GSLS-model-based scheme has the advantage of parallel computation when solved using the staggered-grid finite-difference (SGFD) method[37,38]. Nevertheless, the GSLS model requires internal memory variables, which could significantly increase the computation time and memory, especially in 3D cases[39,40]. In contrast, the recently developed decoupled fractional Laplacians (DFL) equation is an ideal propagator for Rayleigh waves in attenuation media[41,42]. Compared with the time-fractional viscoelastic wave equation[43], the DFL equation avoids a large amount of wavefield storage, thus benefiting from higher computational efficiency[44].

The transfer matrix method, or equivalently the stiffness matrix method, has proven effective in studying wave propagation in multilayered media. These methods correlate the transformed response at the bottom of a layer, expressed as a transfer matrix or stiffness matrix, with a corresponding quantity at the top of a lower layer. The drawback of these methods is their substantial memory requirement and computational effort, and they are prone to errors due to the treatment of infinite boundaries when the solution is numerically evaluated, having been converted from the frequency-wavenumber domain to the time-spatial domain. To address these limitations, the thin layer method, an approximation to the stiffness matrix method, expands the transcendental functions in an exact stiffness matrix in terms of layer thickness, considering terms up to the second order of layer thickness. Compared to the stiffness method, the thin layer method results in mathematically more manageable stiffness matrices that involve only quadratic functions rather than transcendental functions, thus enhancing computational efficiency. In 1970, scholar Lysmer[45] first applied the thin layer stiffness matrix method to derive the coefficient equation of Rayleigh waves and analyze their propagation characteristics in the upper laminated soil layer of bedrock. Lysmer obtained the group velocity and dispersion curve of surface waves. Subsequently, several scholars utilized the thin-layer method to study P-SV waves and SH waves. However, the accuracy of the calculation results was not satisfactory[46]. To achieve necessary accuracy, the thin layer method requires layer thickness to be small in a sense of the smallest relevant wavelength. It implements such a requirement by dividing a thick layer into many thin layers of artifact. In 1981, Kausel and Peek[47] derived the layered stiffness matrix, enabling the direct calculation of eigenvalues using the stiffness matrix for P-SV waves in layered media. This approach proved to be fast and accurate in calculations.

Previous studies have explored the effects of anisotropy and viscoelasticity on Rayleigh waves, leading to the development of various numerical and analytical methods[15–26]. However, these studies often focus on specific scenarios or media types, and there remains a gap in comprehensive research on the accurate synthesis of Rayleigh wave fields in both uniform elastic half-spaces and horizontally layered elastic half-spaces. The purpose of this work is to study the phase velocity and mode of Rayleigh wave fields in horizontally layered elastic half-spaces. In this paper, we developed a self-programmed FORTRAN code to simulate the Rayleigh-wave in the half-space models and the layered models by the thin layer stiffness matrix method. First, we introduced the methodology, which involves the wave equations, the boundary treatments, and the modeling scheme. Then, in the homogeneous half-space models, we tested the modeling program against the elastic analytical solution in time domain, verified the correctness of modeling results via comparing with the theoretical phase velocities of Rayleigh-wave. Finally, in the layered models including the two-layer models and multi-layer models, we further investigated the performance of our FORTRAN language codes in modeling Rayleigh-wave, and analyzed the characteristics of Rayleigh waves in the layered media, as well as verify the computational efficiency of the self-programmed FORTRAN program. This study extends our previous research on the three-dimensional time-domain partitioned analysis of soil-structure interaction (PASSI) under P-SV and SH waves[48–50], aiming to enhance the PASSI method's capabilities to analyze SSI under the influence of Rayleigh waves.

Rayleigh wave field in elastic half-space

Basic principle

Rayleigh wave velocity

The general solution for the rightward-propagating harmonic of in-plane P-SV surface waves[51] can be expressed as

$$\varphi = E_p e^{i(\omega t - k_1 x_1 + k_{2p} x_2)} + F_p e^{i(\omega t - k_1 x_1 - k_{2p} x_2)} \tag{1}$$

$$\psi = E_s e^{i(\omega t - k_1 x_1 + k_{2s} x_2)} + F_s e^{i(\omega t - k_1 x_1 - k_{2s} x_2)} \tag{2}$$

where φ and ψ represent the displacement potentials for P-waves and SV-waves, respectively, where $\omega > 0$ and $k_1 > \omega/c_s$. The parameter c denotes the propagation speed of P-SV surface waves along the x_1 axis, with $c = \omega/k_1$ and $c < c_s$. Here, ω denotes the angular frequency.

The first term in Eqs. (1) and (2) increases with depth x_2 and does not represent surface wave behavior, so it should be omitted. Therefore, the analytic expression for P-SV surface waves can be written as

$$\varphi = F_p e^{i(\omega t - k_1 x_1 - k_{2p} x_2)} \tag{3}$$

$$\psi = F_s e^{i(\omega t - k_1 x_1 - k_{2s} x_2)} \tag{4}$$

here,

$$k_{2p} = -i\sqrt{k_1^2 - \left(\frac{\omega}{c_p}\right)^2} \tag{5}$$

$$k_{2s} = -i\sqrt{k_1^2 - \left(\frac{\omega}{c_s}\right)^2} \tag{6}$$

In Eqs. (5) and (6), the square roots are taken as arithmetic roots. Substitute Eqs. (3) and (4) into the following free boundary conditions:

$$(\lambda + 2\mu)\,\varphi_{ii} - 2\mu\,(\psi_{12} - \varphi_{11}) = 0 \tag{7}$$

$$\mu\,(2\varphi_{12} - \psi_{11} + \psi_{22}) = 0 \tag{8}$$

And modified the above equations to:

$$2i\sqrt{1 - \left(\frac{c}{c_p}\right)^2} F_p + \left(2 - \frac{c^2}{c_s^2}\right) F_s = 0 \tag{9}$$

$$\left(2 - \frac{c^2}{c_s^2}\right) F_p - 2i\sqrt{1 - \left(\frac{c}{c_s}\right)^2} F_s = 0 \tag{10}$$

In the equations, $c = \omega/k_1$. For Eqs. (9) and (10) to have non-zero solutions for F_s and F_p, the wave speed c must satisfy the condition that makes the determinant of the coefficient matrix in Eqs. (9) and (10) equal to zero.

$$\left(2 - \frac{c^2}{c_s^2}\right)^2 = 4\sqrt{1 - \frac{c^2}{c_p^2}}\sqrt{1 - \frac{c^2}{c_s^2}} \tag{11}$$

Squaring both sides of Eq. (11) yields:

$$\frac{c^2}{c_s^2}\left[\frac{c^6}{c_s^6} - 8\frac{c^4}{c_s^4} + c^2\left(\frac{24}{c_s^2} - \frac{16}{c_p^2}\right) - 16\left(1 - \frac{c_s^2}{c_p^2}\right)\right] = 0 \tag{12}$$

The non-zero solutions that satisfy the condition can be approximated as:

$$c/c_s = (0.87 + 1.12\nu)/(1 + \nu) \tag{13}$$

It follows that the Rayleigh wave velocity c is independent of frequency and depends on the shear wave speed c_s and Poisson's ratio ν. Therefore, in a homogeneous elastic half-space, the shape of Rayleigh waves remains unchanged during propagation, making them a type of non-dissipative wave.

Rayleigh wave form

The displacement components for the 2D wave propagation problem in a plane are:

$$u_1 = \frac{\partial \varphi}{\partial x_1} + \frac{\partial \psi}{\partial x_2} \tag{14}$$

$$u_2 = \frac{\partial \varphi}{\partial x_2} - \frac{\partial \psi}{\partial x_1} \tag{15}$$

By substituting Eqs. (3) and (4) into Eqs. (14) and (15), and combining with Eqs. (9) and (10), the displacement field of the Rayleigh wave can be obtained.

$$u_1 = U_1(\omega, x_2)\, e^{i\left(\omega t - \frac{\omega}{c} x_1\right)} \tag{16}$$

$$u_2 = U_2(\omega, x_2)\, e^{i\left(\omega t - \frac{\omega}{c} x_1\right)} \tag{17}$$

Analytical solution 1

According to Liao's related theory[51–53], consider the displacement of Rayleigh waves in a uniform elastic half-space as

$$u_i = u_i(\zeta, x_2), i = 1, 2 \tag{18}$$

where $\zeta = t - x_2/c$,the horizontal displacement time of a point (0,0) (as shown in Fig. 1) on the free surface $u_1(t, 0) = u_0(t)$ is known, and the Fourier transform can be used to construct the displacement time $u_i(\zeta, x_2), i = 1, 2$ of any point in the wave field

$$u_i(\zeta, Z) = \frac{1}{2\pi} \int_{-\infty}^{\infty} U_i(\omega, Z)\, e^{iw\zeta} d\omega = \frac{1}{\pi} \mathrm{Re} \int_{0}^{\infty} U_i(\omega, Z)\, e^{iw\zeta} d\omega \tag{19}$$

$$U_1(\omega, x_2) = A_1(\omega, x_2)\, U_0(\omega) \tag{20}$$

$$U_2(\omega, x_2) = A_2(\omega, x_2)\, U_0(\omega) \cdot (-iD) \tag{21}$$

and,

$$u_1(\zeta, x_2) = \frac{1}{\pi} Re \int_{0}^{\infty} A_1(\omega, x_2)\, U_0(\omega)\, e^{i\omega\zeta} d\omega \tag{22}$$

$$u_2(\zeta, x_2) = -\frac{D}{\pi} Im \int_{0}^{\infty} A_2(\omega, x_2)\, U_0(\omega)\, e^{i\omega\zeta} d\omega \tag{23}$$

here,

$$A_1(\omega, x_2) = \left(1 - 2\frac{c_s^2}{c^2}\right) \exp\left(-\frac{\omega}{c} x_2 \sqrt{1 - \frac{c^2}{c_s^2}}\right) + 2\frac{c_s^2}{c^2} \exp\left(-\frac{\omega}{c} x_2 \sqrt{1 - \frac{c^2}{c_p^2}}\right) \tag{24}$$

$$A_2(\omega, x_2) = \left(1 - 2\frac{c_s^2}{c^2}\right) \exp\left(-\frac{\omega}{c} x_2 \sqrt{1 - \frac{c^2}{c_p^2}}\right) + 2\frac{c_s^2}{c^2} \exp\left(-\frac{\omega}{c} x_2 \sqrt{1 - \frac{c^2}{c_s^2}}\right) \tag{25}$$

$$D = 2\sqrt{1 - c^2/c_p^2} \Big/ \left(2 - c^2/c_s^2\right) \tag{26}$$

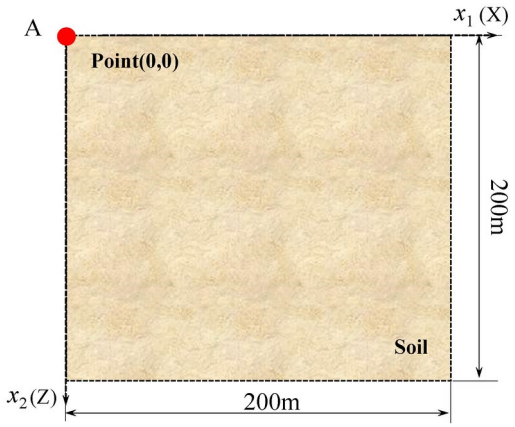

Fig. 1. The half-space site model.

where x_1 represents the displacement along the x-direction, x_2 denotes depth along the z-direction; c, c_s and c_p are the Rayleigh, shear and compressional wave velocities of the site, respectively. In the self-programmed FORTRAN program, the Fast Fourier Transform (FFT) was used to obtain the numerical results of Eqs. (22) and (23).

Analytical solution 2

The Ricker wavelet, a widely used type in seismic exploration, is derived rigorously from the wave equation. Professor Yanghua Wang[54] from Imperial College London has provided an in-depth analysis of the Ricker wavelet. Building on the theoretical methods associated with the Ricker wavelet, a method has been developed to easily obtain the analytical solution for the input wavefield of Rayleigh waves[55]. Let the horizontal displacement component of Rayleigh wave at a point of free surface be

$$u_0(\zeta) = \frac{\zeta_0^2}{\pi} \cdot \frac{\zeta_0^2 - \zeta^2}{\left(\zeta_0^2 + \zeta^2\right)^2}, \quad \zeta_0 > 0 \tag{27}$$

Its frequency spectrum is

$$U_0(\omega) = \zeta_0^2 \omega e^{-\zeta_0 \omega}, \quad \omega > 0 \tag{28}$$

The spectrum reaches its maximum value at $\omega = \omega_0 = 1/\zeta_0$, i.e., its superior frequency is $\omega_0 = 1/\zeta_0$. Therefore, the frequency component of the input ground vibration ζ_0 can be controlled by the choice of parameter $u_0(\zeta)$.

Substituting Eq. (28) into Eqs. (22) and (23), it was obtained that

$$u_1(\zeta, Z) = \frac{\zeta_0^2}{\pi} \left\{ \frac{(\zeta_0 + m_1 Z)^2 - \zeta^2}{\left[\zeta^2 + (\zeta_0 + m_1 Z)^2\right]^2} \cdot A + \frac{(\zeta_0 + m_2 Z)^2 - \zeta^2}{\left[\zeta^2 + (\zeta_0 + m_2 Z)^2\right]^2} B \right\} \tag{29}$$

$$u_2(\zeta, Z) = \frac{-2D\zeta_0^2}{\pi} \left\{ \frac{\zeta_0 + m_2 Z}{\left[\zeta^2 + (\zeta_0 + m_2 Z)^2\right]^2} \cdot A + \frac{\zeta_0 + m_1 Z}{\left[\zeta^2 + (\zeta_0 + m_1 Z)^2\right]^2} B \right\} \cdot \zeta \tag{30}$$

where

$$\begin{aligned} &A = 1 - 2(c_s/c)^2, B = 2(c_s/c)^2 \\ &m_1 = \sqrt{1 - c^2/c_s^2}\Big/ c, m_2 = \sqrt{1 - c^2/c_p^2}\Big/ c \end{aligned} \tag{31}$$

where A, B, m_1, and m_2 represent the relevant parameters.

Algorithm validation

Based on Eqs. (19)–(23), we implemented a FORTRAN program (Analytical solution 1) to obtain the analytical solution for Rayleigh waves in a homogeneous elastic half-space. Additionally, we developed a corresponding program (MATLAB code, Analytical solution 2) based on Eqs. (29)–(31) to compute another analytical solution for Rayleigh waves in the same medium. A comparative analysis was conducted to verify the consistency of the computational results obtained from these two analytical solutions when applied to the same field. The comparison revealed identical results, thus ensuring the accuracy and reliability of the implemented algorithms. Subsequently, the synthesized wave field was utilized as the input for the free field analysis. A wave field simulation was conducted using a finite element program combined with a multiple transmission artificial boundary approach. The correctness of the program was validated by comparing the results obtained from the free field analysis with those obtained from the finite element analysis. Acknowledging the importance of accurately characterizing the Rayleigh wave field in practical applications, this verification process served to validate the implemented FORTRAN program, ensuring its fidelity and suitability for further analyses.

Model and parameters

In Fig. 2, the calculation area of the two-dimensional uniform elastic half-space is 200 m × 200 m, and the soil material parameters are presented in Table 1. The soil was discretized into 1.0 m × 1.0 m quadrilateral four-node elements in the x- and z-directions, comprising a total of 40,000 elements and 40,401 nodes. For site analysis, observation points A (0,0), B (50,50), and C (100,100) are illustrated in Fig. 2.

Figure 3 depicts the acceleration time history and Fourier spectrum of the motion. To facilitate a comprehensive comparison between the two analytical solutions, we generated the pulse waveform displayed in Fig. 3 as the input wave by applying Eqs. (8) and (9) with a value of $\zeta_0 = 0.05$. The input wave is vertically introduced from the bottom of the bedrock, with a total duration of 3.2738 s and a cut-off frequency approximately 3.18 Hz. This was done through Fourier transform analysis, where UF1 represents the spectrum obtained by Fourier transform in MATLAB for the pulse timescale, and UF2 represents each frequency point used in wave creation.

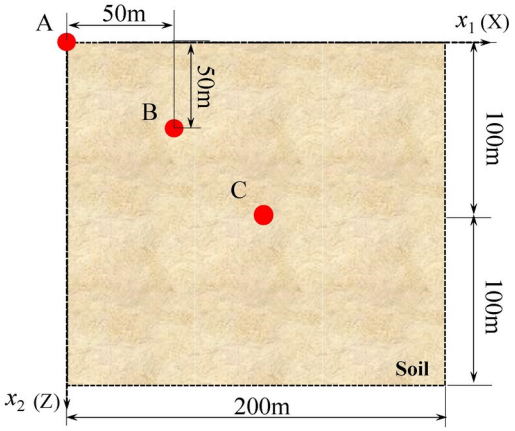

Fig. 2. Homogeneous elastic half-space site model.

Density (kg/m^3)	Modulus of elasticity (Pa)	Poisson's ratio	Rayleigh wave velocity (m/s)	Shear wave velocity (m/s)
1000	3.0×10^8	0.25	370	400

Table 1. Soil parameters.

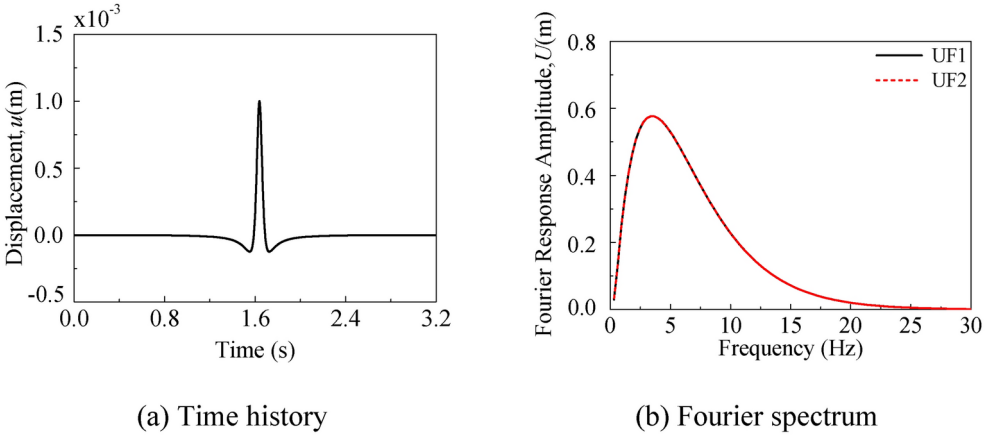

Fig. 3. Input impulse wave.

Results analysis

To solve the site, a custom program written in FORTRAN was utilized, and three observation points displayed in Fig. 2 were selected, as demonstrated in Figs. 4 and 5. Upon comparing the results, it was observed that the computed values obtained from both solution methods exhibit complete agreement, thereby providing initial validation of the accuracy of the approach applied in this paper for solving the uniform elastic half-space Rayleigh wave field.

The site was simulated using a finite element program incorporating multiple transmission artificial boundaries, with the analytical solution employed as the input for the free field. Moreover, the results from the three observation points depicted in Fig. 2 were selected for comparative analysis, as presented in Figs. 6 and 7. Notably, a precise agreement was observed between the finite element results and the free field results, thereby providing further validation of the accuracy and correctness of the implemented program.

The properties of Rayleigh wave field

Rayleigh waves are surface waves that propagate along the interface between two distinct media, commonly the surface and subsurface. Characterized by an elliptical particle motion, these waves involve simultaneous vertical and horizontal particle displacements. Rayleigh waves hold particular significance in seismic exploration due to their role in conveying valuable information about the subsurface structure and properties. In earthquake engineering, a comprehensive analysis of Rayleigh wave propagation is crucial for assessing site response and for the design of structures capable of withstanding seismic forces.

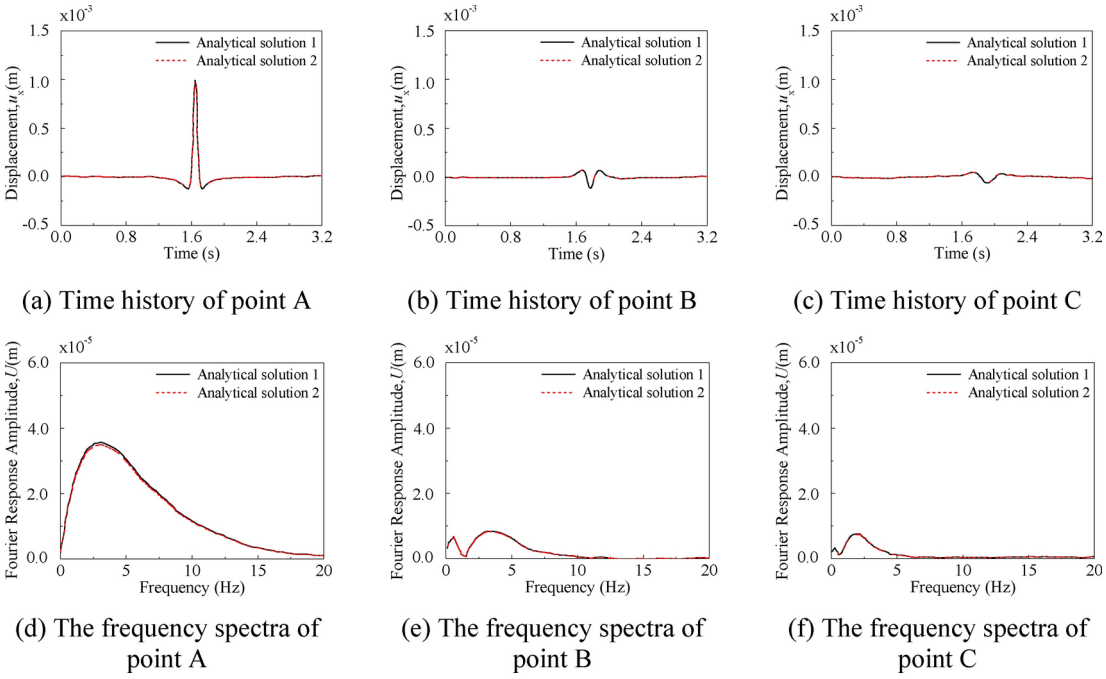

Fig. 4. The responses of each observation point in x-direction (x_1-direction).

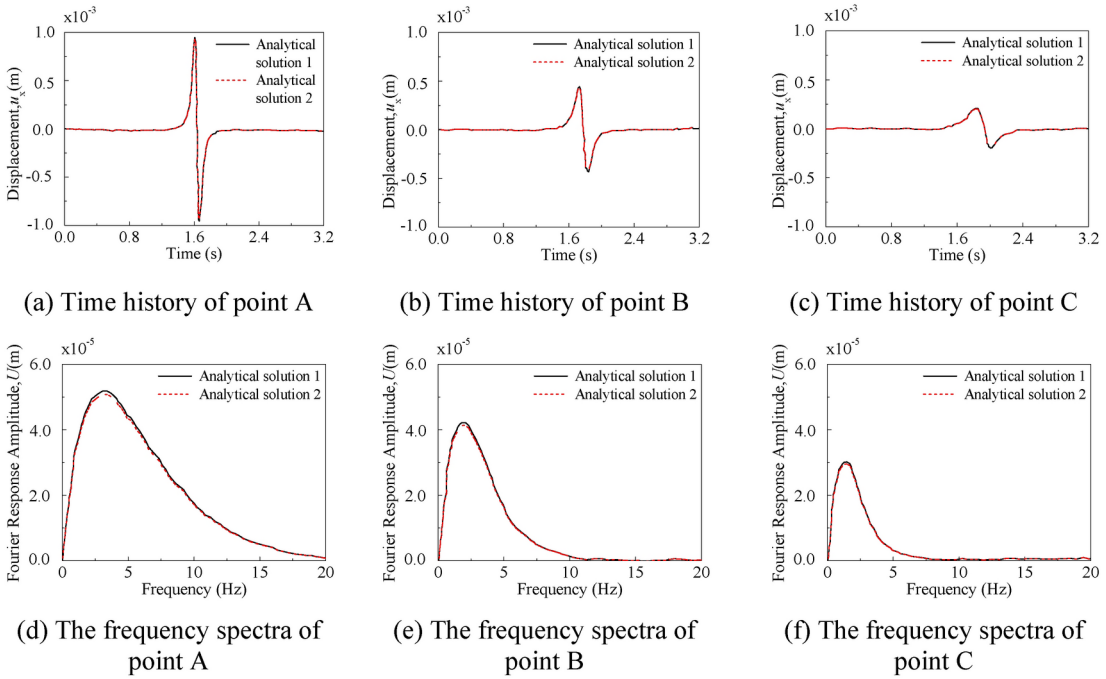

Fig. 5. The responses of each observation point in z-direction (x_2-direction) (Compared with the two analytical solutions).

In this study, based on the response results in the x-direction and z-direction, a total of 12 points within the site were selected, and the trajectory of the mass points was plotted, as illustrated in Fig. 8. From Fig. 8, it is evident that the trajectory of the mass at the free surface of the soil follows a clockwise elliptical pattern. The elliptical motion at the free surface is a result of the superposition of vertical and horizontal components of the Rayleigh wave particle motion. Meanwhile, the clockwise rotation at the surface indicates that the vertical component of motion leads the horizontal component. As the depth increases, the elliptical trajectory gradually narrows, eventually transitioning into a counterclockwise ellipse until both the horizontal and vertical motion

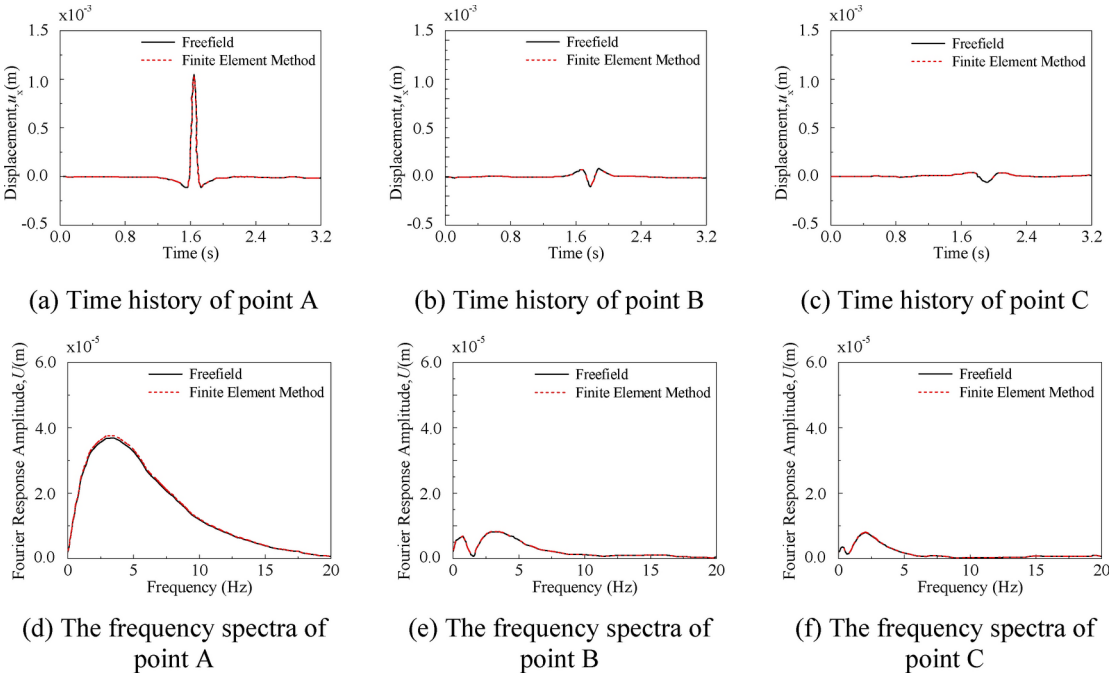

Fig. 6. The responses of each observation point in x-direction (x_1-direction).

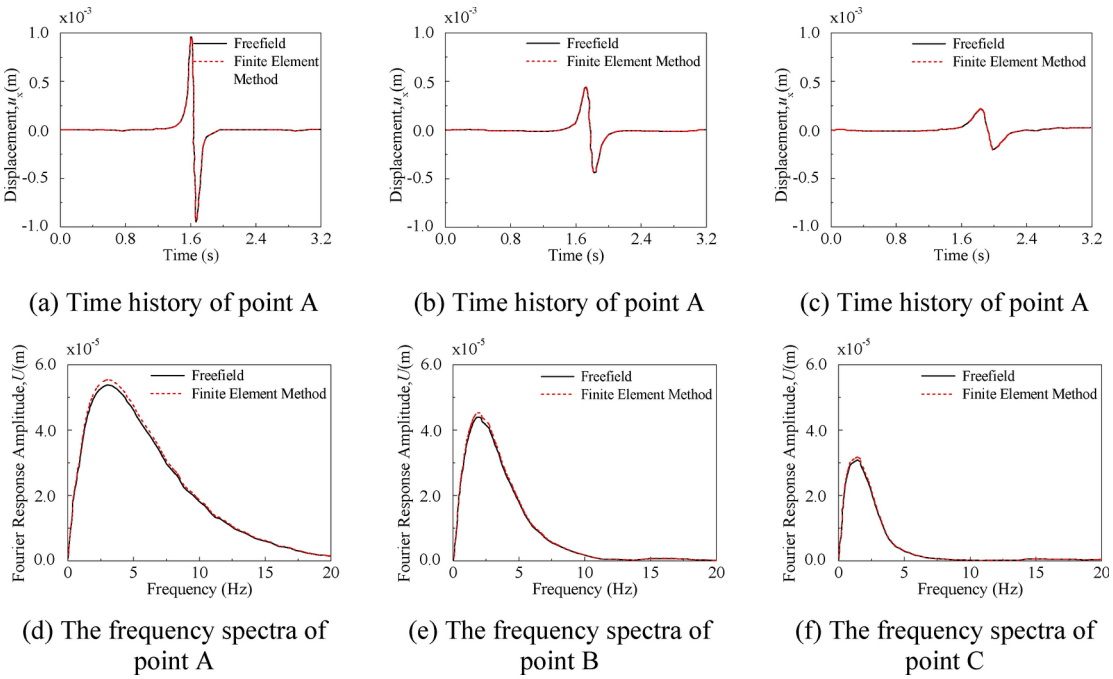

Fig. 7. The responses of each observation point in z-direction (x_2-direction).

components approach zero. This change in direction is due to the decrease in the amplitude of the horizontal component relative to the vertical component. In the horizontal direction, the trajectory remains consistent, aligning with the distinctive wave characteristics of Rayleigh waves.

Based on the propagation characteristics of Rayleigh waves, Rayleigh wave response with a frequency of 10 Hz was selected, and horizontal and vertical displacement curves of Rayleigh waves with depth were plotted, as depicted in Fig. 9. This figure presents the variation of A_2 and A_1/D with depth, where the horizontal coordinate is X/λ, and $\lambda = 2\pi c/\omega$ denotes the Rayleigh wave wavelength. The vertical coordinates represent the ratio of the vertical and horizontal displacements along the depth to the vertical and horizontal displacements of the free surface point for A_2 and A_1/D, respectively. As the depth increases, the vertical component amplitude (A_2) initially

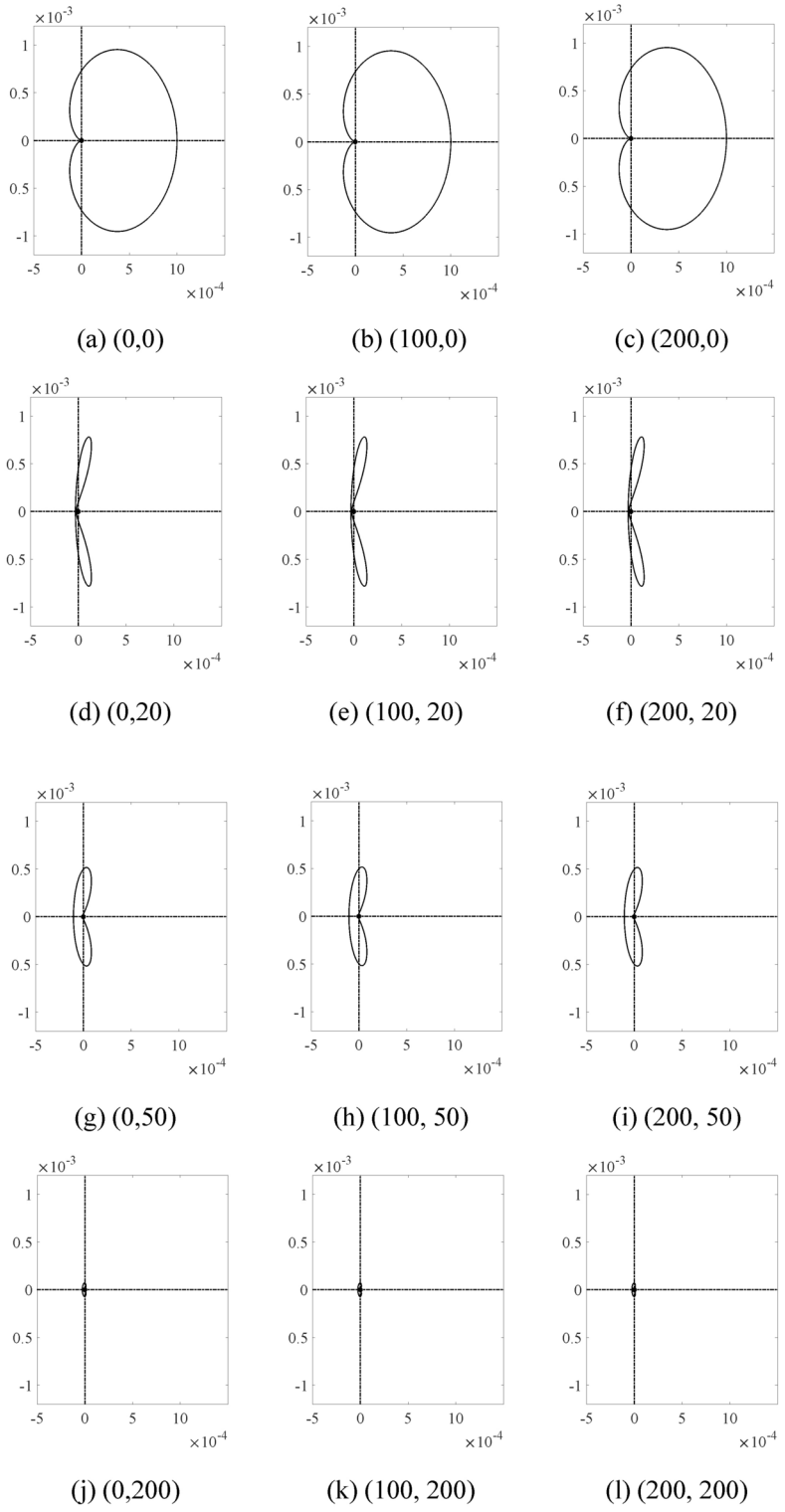

Fig. 8. Trajectory of points in the uniform elastic half-space Rayleigh wave field.

increases slightly due to the focusing effect of the wave. However, it then decreases and eventually approaches zero, indicating the attenuation of the wave with depth. In contrast, the horizontal component amplitude (A_1/D) decays more rapidly with depth. This is because the horizontal component of the Rayleigh wave is more sensitive to the properties of the subsurface layers. Ultimately, both horizontal and vertical components tend towards zero, indicating that fluctuation energy is mainly concentrated within one wavelength range.

To illustrate the propagation characteristics of Rayleigh waves in a homogeneous elastic half-space more effectively, a wavefield diagram is presented in Fig. 10. The diagram illustrates the displacement time history

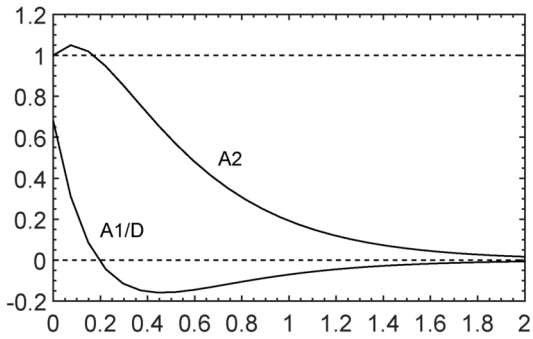

Fig. 9. Variation of horizontal and vertical mass displacement of Rayleigh waves with depth x_2.

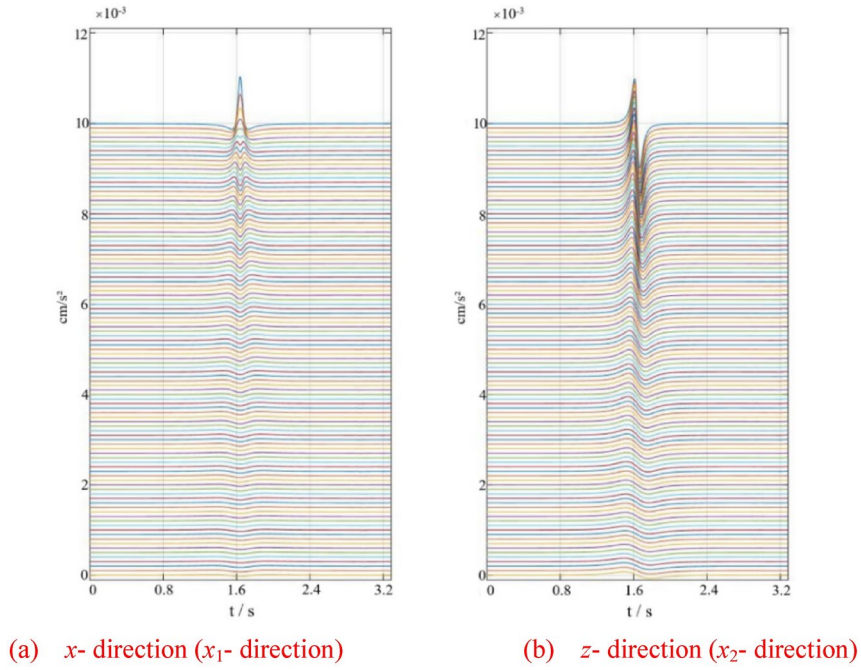

Fig. 10. Uniform elastic half-space Rayleigh wave field time course diagram.

at various depths along the *x*-direction. The diagram displays displacement timescales for 101 points along the depth direction, starting from zero and incrementing in 2 m intervals up to a depth of 200 m. Upon observing the graph, it becomes evident that the displacement in the *x*-direction rapidly decreases to zero as the depth increases. Subsequently, it reverses its direction, reaching a certain value before gradually diminishing back to zero. Conversely, the displacement in the z-direction decreases at a slower rate compared to the x-direction and does not exhibit any reverse direction motion. The decay rate of the *x*-direction displacement is faster than that of the *z*-direction, ultimately leading to both responses approaching zero at a depth of 200 m. This observation indicates that the Rayleigh wave energy is predominantly concentrated near the surface and decays more rapidly in the horizontal direction compared to the vertical direction.

We analyzed the faster decay rate of the *x*-direction displacement compared to the *z*-direction and its implications for wave propagation and site response. Figure 11 illustrates the response from the entire site at twelve specific time instances: t = 1.6384 s, t = 1.7184 s, t = 1.7984 s, t = 1.8784 s, t = 1.9584 s, t = 2.0384 s, t = 2.1184 s, t = 2.1984s, t = 2.2784 s, t = 2.3584 s, t = 2.4384 s, and t = 2.5184 s. These moments capture the wavefield clouds in the x- and z-directions. The plots showcase that the waveforms of Rayleigh waves remain constant throughout their propagation. Additionally, the energy is predominantly concentrated near the surface in the depth direction. It is notable that the decay rate of displacement is more pronounced along the *x*-direction compared to the *z*-direction as depth increases.

As the decay of Rayleigh waves along depth is measured in wavelengths, it is theoretically expected that higher frequency waves decay first. To account for this, a FORTRAN program was utilized to generate pulses that are constant in the 0–20 Hz range on the spectrum and zero at other frequency points, as depicted in Fig. 12. The two coincide perfectly, verifying the accuracy of the wave creation procedure.

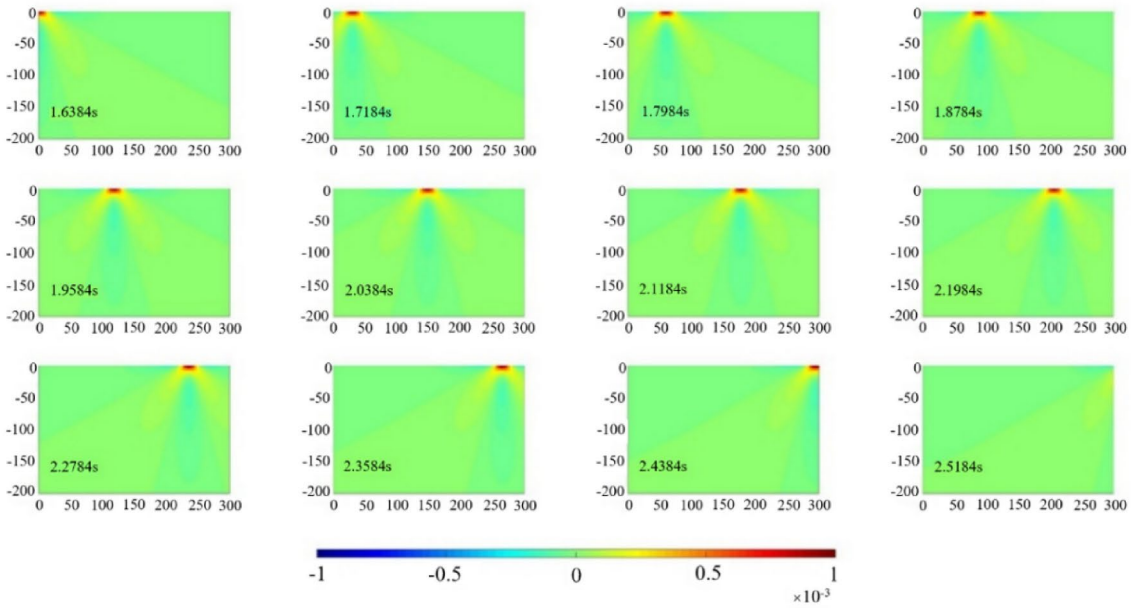

(a) x-direction (x_1- direction)

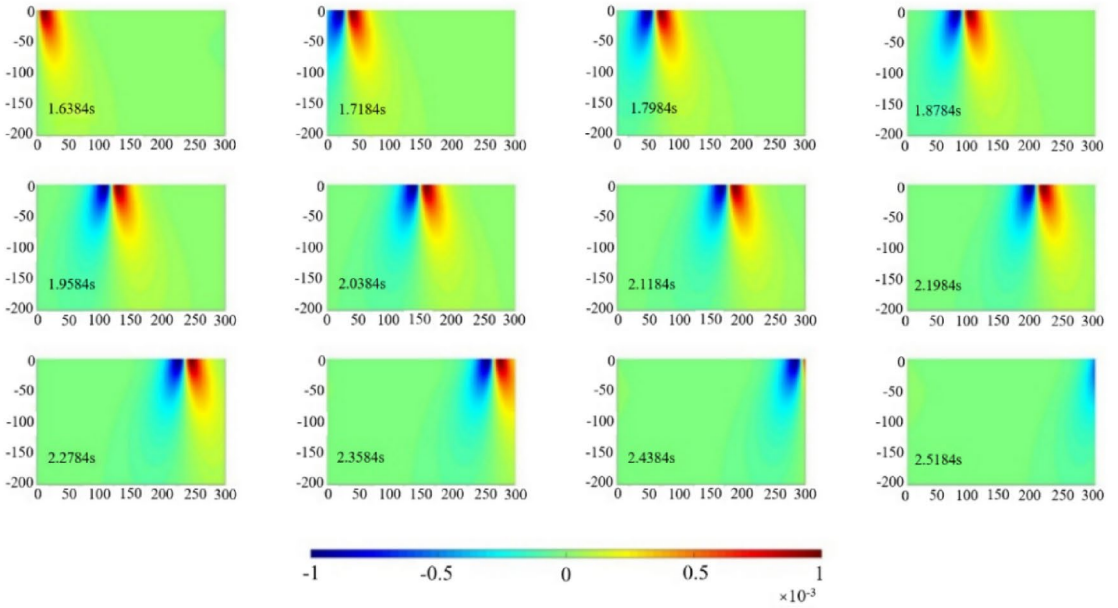

(b) z-direction (x_2- direction)

Fig. 11. Uniform elastic half-space Rayleigh wave field cloud.

In this study, the wave field of the pulse shown in Fig. 12 was solved using a self-programmed analytical solution procedure, which served as a free field for wave field analysis by finite element method. We discussed the frequency dependency of Rayleigh wave attenuation using the input pulse and frequency spectrum presented in Fig. 12. We can find that higher frequency components of the Rayleigh wave decay faster with depth due to their shorter wavelengths and higher sensitivity to subsurface properties. This observation is consistent with theoretical expectations and provides valuable insights into the relationship between frequency and wave attenuation.

Figures 13 and 14 illustrated the responses of three points with coordinates (0,0), (50,50), and (100,100) respectively, as shown in Fig. 1. It can be observed that as depth increases, high frequency Rayleigh waves decay faster along the z-direction. In the x-direction, the Rayleigh waves exhibit a pattern of decreasing, increasing, and then decreasing again from high to low frequencies due to the inverse increasing property of mass motion. This

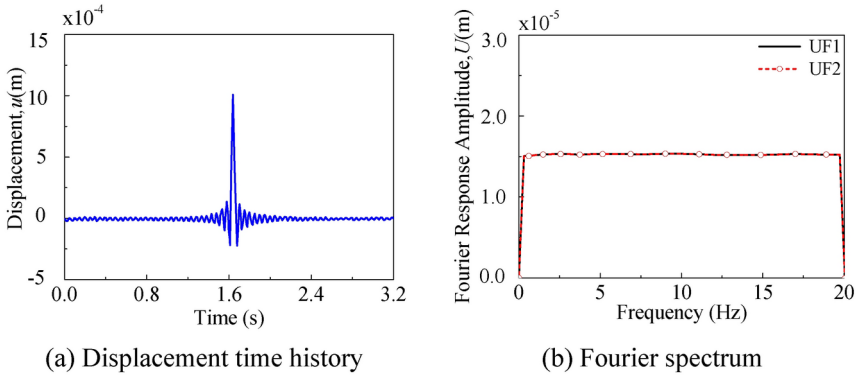

(a) Displacement time history (b) Fourier spectrum

Fig. 12. Input pulse (Rayleigh wave decay along depth versus frequency).

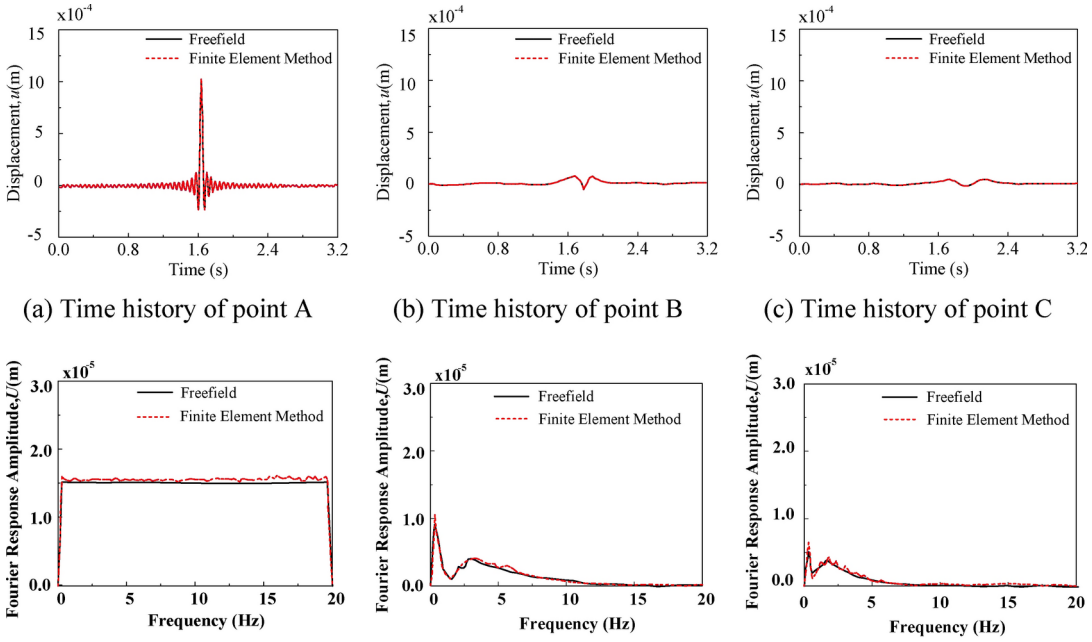

(a) Time history of point A (b) Time history of point B (c) Time history of point C

(d) The frequency spectra of point A (e) The frequency spectra of point B (f) The frequency spectra of point C

Fig. 13. The responses of each observation point in x-direction (x_1-direction). (Relation between attenuation of Rayleigh wave along depth direction and frequency).

is due to the inverse relationship between frequency and particle motion, where higher frequencies correspond to smaller particle motion amplitudes.

Rayleigh wave fields in horizontally stratified elastic half-spaces

When the shear wave velocity of a layered medium is lower than that of the underlying semi-infinite space, Rayleigh waves with the same frequency exhibit varying propagation velocities and wavelengths. In other words, there are multiple propagation modes for Rayleigh waves at the same frequency. The higher the phase velocity, the higher the order of the mode for a given frequency. All modes, except for the fundamental mode (first-order mode), have a cut-off frequency. A mode will only appear if its frequency is above the cut-off frequency. Therefore, as the frequency increases, more modes become available. The curve depicting the relationship between the phase velocity and frequency of a mode is referred to as the dispersion curve. It provides information about the stratification of the site. Consequently, solving the dispersion curves for Rayleigh waves plays a crucial role in geophysical exploration.

Currently, there exist various computational methods for calculating Rayleigh wave fields in horizontally layered elastic half-spaces. The two most common methods are the rapid scalar method and the thin layer stiffness method. Qin et al.[56] compared the advantages and disadvantages of these two methods and found

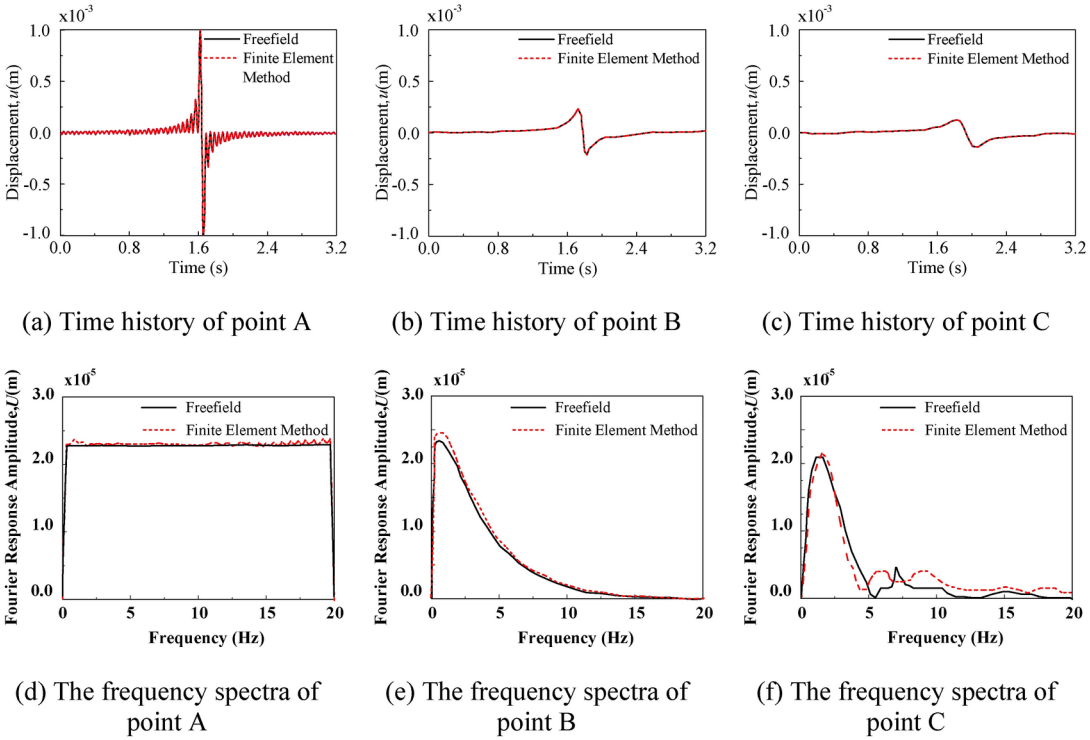

Fig. 14. The responses of each observation point in z-direction (x_2-direction). (Relation between attenuation of Rayleigh wave along depth direction and frequency).

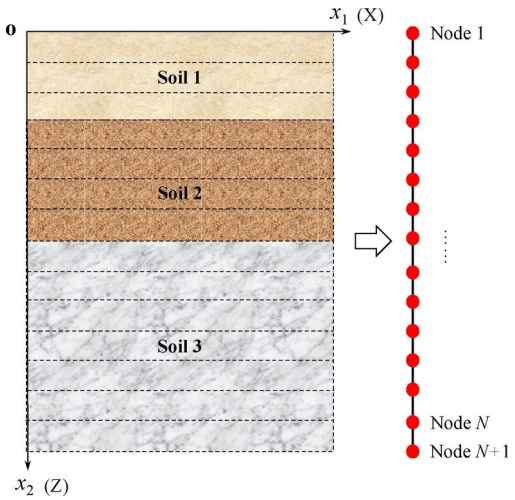

Fig. 15. Simplified model for calculating rayleigh wave field by thin layer stiffness method.

that the overall trend of the dispersion curve results obtained by both methods is consistent. However, the thin layer stiffness method exhibits better performance in calculating the dispersion curves at lower frequencies. Considering that seismic waves predominantly consist of low-frequency waves below 50 Hz, this study employs the thin layer stiffness method to compute the Rayleigh wave field in a horizontally layered elastic half-space.

Dispersion curve

As depicted in Fig. 15, the calculation of a horizontally stratified site is initially simplified into a one-dimensional model. Subsequently, N elements and $N+1$ nodes are generated by dividing the model into discrete elements.

For small element sizes relative to the wavelength, the stratification stiffness can be approximated as follows:

$$K = A\mathrm{k}^2 + B\mathrm{k} + G - \omega^2 M \tag{32}$$

where

$$A = \frac{d}{6}\begin{bmatrix} 2(\lambda+2\mu) & 0 & \lambda+2\mu & 0 \\ 0 & 2\mu & 0 & \mu \\ \lambda+2\mu & 0 & 2(\lambda+2\mu) & 0 \\ 0 & \mu & 0 & 2\mu \end{bmatrix} \tag{33}$$

$$B = \frac{1}{2}\begin{bmatrix} 0 & \lambda-\mu & 0 & -\lambda-\mu \\ \lambda-\mu & 0 & \lambda+\mu & 0 \\ 0 & \lambda+\mu & 0 & -\lambda+\mu \\ -\lambda-\mu & 0 & -\lambda+\mu & 0 \end{bmatrix} \tag{34}$$

$$G = \frac{1}{d}\begin{bmatrix} \mu & 0 & -\mu & 0 \\ 0 & \lambda+2\mu & 0 & -(\lambda+2\mu) \\ -\mu & 0 & \mu & 0 \\ 0 & -(\lambda+2\mu) & 0 & \lambda+2\mu \end{bmatrix} \tag{35}$$

$$M = \frac{\rho d}{6}\begin{bmatrix} 2 & 0 & 1 & 0 \\ 0 & 2 & 0 & 1 \\ 1 & 0 & 2 & 0 \\ 0 & 1 & 0 & 2 \end{bmatrix} \tag{36}$$

Here, d, λ and μ are the layer thicknesses, Lamé constants and shear moduli of the corresponding thin layers, respectively, and the above four matrices are real symmetric matrices. In 2005, Kausel's "mass lumping" pointed out that equivalence of Eq. (37) can be used to replace Eq. (36)

$$M = \frac{\rho d}{6}\begin{bmatrix} 3 & 0 & 0 & 0 \\ 0 & 3 & 0 & 0 \\ 0 & 0 & 3 & 0 \\ 0 & 0 & 0 & 3 \end{bmatrix} \tag{37}$$

Integrating the element stiffness array according to the stress–strain continuity condition yields that

$$\left(\tilde{A}k^2 + \tilde{B}k + \tilde{G}\right)\tilde{U} = \omega^2\tilde{M}\tilde{U} \tag{38}$$

where $\tilde{A}$, $\tilde{B}$, $\tilde{G}$ and $\tilde{M}$ are combined by the thin layer stiffnesses of Eqs. (33)–(35) and (37) respectively, and

$$\tilde{U} = \left[u_0, \omega_0, u_1, \omega_1, \ldots, u_{N-2}, \omega_{N-2}, u_{N-1}, \omega_{N-1}\right]^T \tag{39}$$

For Eq. (38), when a value ω is given, it becomes a problem of finding quadratic eigenvalues for k, which is difficult to solve, and therefore, by introducing an intermediate variable $a = k\tilde{U}$ it is obtained that

$$k\begin{bmatrix} I & 0 \\ 0 & \tilde{G} \end{bmatrix}\begin{bmatrix} \tilde{U} \\ a \end{bmatrix} = \begin{bmatrix} 0 & I \\ \omega^2\tilde{M} - \tilde{A}^2 & -\tilde{B} \end{bmatrix}\begin{bmatrix} \tilde{U} \\ a \end{bmatrix} \tag{40}$$

Using Eq. (40), the quadratic eigenvalue problem is converted into a primary eigenvalue problem.

It follows that there should be $4N$ sets of eigenvalues and eigenvectors. However, not all sets of eigenvalues and eigenvectors need to be considered. For computational efficiency, only the first n modal orders are typically calculated. Since the largest eigenvalue corresponds to the smallest phase velocity, which represents the fundamental mode, only the n consecutive eigenvalues and their corresponding eigenvectors that are smaller than or equal to the fundamental mode need to be computed. The phase velocity of the fundamental mode is obtained through the arithmetic square root of the smallest root of Eq. (41).

$$\frac{1}{v_s^6}x^3 - \frac{8}{v_s^4}x^2 + \left(\frac{24}{v_s^2} - \frac{16}{v_p^2}\right)x - 16\left(1 - \left(\frac{v_s}{v_p}\right)^2\right) = 0 \tag{41}$$

where v_s and v_p correspond to the transverse wave velocity and longitudinal wave velocity of the minimum transverse wave velocity soil layer.

After solving the characteristic equations by a self-programmed program in FORTRAN language, the phase velocity and group velocity can be obtained by the following equations

$$v_{phase} = \omega/k \tag{42}$$

$$v_{group} = \frac{\delta\omega}{\delta k} = \frac{\tilde{U}^T (2kG + B)\,\tilde{U}}{2\omega \tilde{U}^T M \tilde{U}} \tag{43}$$

The wavefield we want can be synthesized by self-programmed in the FORTRAN language according to the independent propagation of the different modes with their corresponding phase velocities.

To meet the accuracy requirements, each mode at each frequency must satisfy the following two points.

(1) Model depth should be deep enough

The model depth is required to be at least twice the maximum sensitivity depth. That is

$$L > 2 \times 0.5\ \mathrm{ml} = \mathrm{ml} \tag{44}$$

where *m* represents the modal order, *l* is the wavelength, and *L* is the model depth.

(2) Element thickness should be small enough

At all depths greater than the maximum sensitivity depth, the wavelength should be greater than 5 times the cell thickness. That is

$$l > 5h_s \tag{45}$$

In the expression, *l* represents the wavelength and h_s represents the sum of the thicknesses of all the elements below the maximum sensitivity depth.

Furthermore, it should be noted that not all modes obtained satisfy the geometric attenuation characteristics of Rayleigh waves. To determine if a mode satisfies the depth-wise attenuation of Rayleigh waves, the vertical displacement of each particle is examined. If the depth-wise displacement attenuates faster than linearly, i.e., if the ratio of the integral of the attenuation function for the upper half of the model to that of the lower half is greater than three, then the mode is considered a valid Rayleigh wave mode. Otherwise, the mode should not be included in the set of required modes.

Modal displacement

The relative displacement of each mode at a specific frequency point can be determined by normalizing the obtained modes at that frequency point as discussed in the previous subsection. The normalization process involves rewriting the stiffness arrays *DA* and *DB* as follows:

$$DA = \frac{d}{6}\begin{bmatrix} 2(\lambda+2\mu) & \lambda+2\mu & & \\ \lambda+2\mu & 2(\lambda+2\mu) & & \\ & & 2\mu & \mu \\ & & \mu & 2\mu \end{bmatrix} = \begin{bmatrix} DA_x & 0 \\ 0 & DA_z \end{bmatrix} \tag{46}$$

$$DB = \frac{1}{2}\begin{bmatrix} & & \lambda-\mu & -\lambda-\mu \\ & & \lambda+\mu & -\lambda+\mu \\ \lambda-\mu & \lambda+\mu & & \\ -\lambda-\mu & -\lambda+\mu & & \end{bmatrix} = \begin{bmatrix} 0 & DB_{xz} \\ DB_{xz}^T & 0 \end{bmatrix} \tag{47}$$

$$\widetilde{U} = [u_0, \omega_0, u_1, \omega_1, \ldots, u_{N-2}, \omega_{N-2}, u_{N-1}, \omega_{N-1}]^T \tag{48}$$

Based on the eigenvalues *k* and eigenvectors $\widetilde{U}$ derived for each mode at a given frequency, the intermediate variables are constructed

$$S = \begin{bmatrix} DA_x & 0 \\ DB_{xz}^T & DA_x \end{bmatrix} \tag{49}$$

$$yz = [ku_0, ku_1, \ldots, ku_{N-2}, ku_{N-1}, \omega_0, \omega_1, \ldots, \omega_{N-2}, \omega_{N-1}] \tag{50}$$

$$zy = [u_0, u_1, \ldots, u_{N-2}, u_{N-1}, k\omega_0, k\omega_1, \ldots, k\omega_{N-2}, k\omega_{N-1}] \tag{51}$$

$$kzy = yz \cdot S \cdot zy^T \tag{52}$$

$$k\_beta = sqrt(kzy/k) \tag{53}$$

The normalized displacement of each mode can be solved for,

$$U_x = \widetilde{U}_x / k\_beta \tag{54}$$

$$U_z = \widetilde{U}_z / k\_beta \tag{55}$$

Material number	Soil layer thickness	Density (kg/m^3)	Modulus of elasticity (Pa)	Poisson's ratio (μ)	Rayleigh wave velocity (m/s)	Shear wave velocity (m/s)	Compression velocity (m/s)
②	100 m	1000	1.0×10^8	0.25	370	400	700
③	100 m	1200	3.0×10^8	0.25	475	516	894

Table 2. Horizontal layer-forming elastic half-space soil parameters.

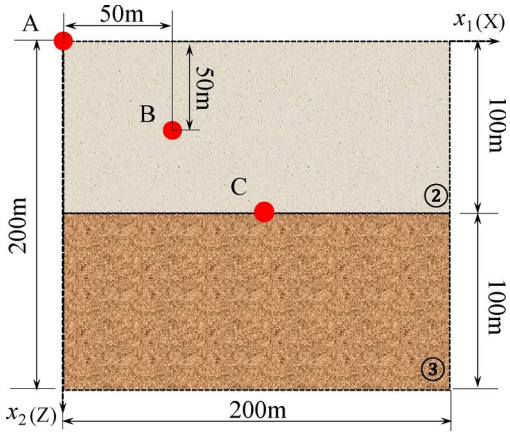

Fig. 16. Horizontal stratified elastic half-space site model.

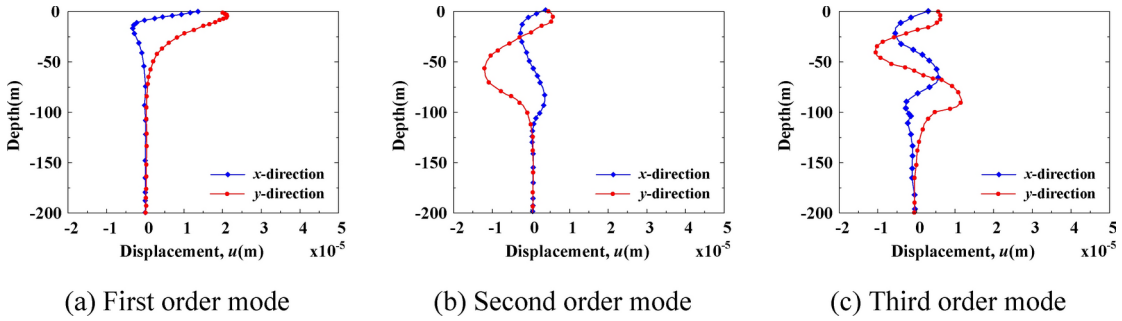

Fig. 17. Modes at 10 Hz. (two-layer soil site).

For a given pulse waveform, it is first transformed into a frequency spectrum using Fourier transform. The displacement of each mode is then computed at every frequency point. After normalization, the displacement of each mode at a specific frequency is multiplied by its corresponding absolute displacement coefficient to obtain the wave field response at that frequency. The array of each mode propagates independently in the site according to its corresponding phase velocity. Finally, the total response of the site is obtained through adding the responses at all frequency points.

Validations of an analytical algorithm for horizontal layered elastic half-space Rayleigh wave fields

Two-layer soil wave field analysis

Building upon the fundamental principles outlined in Section "Basic Principle", we developed a FORTRAN programs to synthesize the Rayleigh wave field in a horizontally layered elastic half-space. The results were inputted as the free field for our simulations, which were conducted using a finite element program and multiple transmission artificial boundary. By comparing the free field and finite element results, we were able to verify the accuracy of our programs.

A two-dimensional, 200 m × 200 m horizontal layered elastic half-space site was created, with media parameters for each layer detailed in Table 2 and shown in Fig. 16. The soil was discretized into quadrilateral four-node elements measuring 1.0 m × 1.0 m in the x- and z-directions, totaling 40,000 elements and 40,401 nodes. The input pulses depicted in Fig. 3 were utilized for this example, with a calculation step count of 32,768 steps and an excitation frequency of 3.18 Hz.

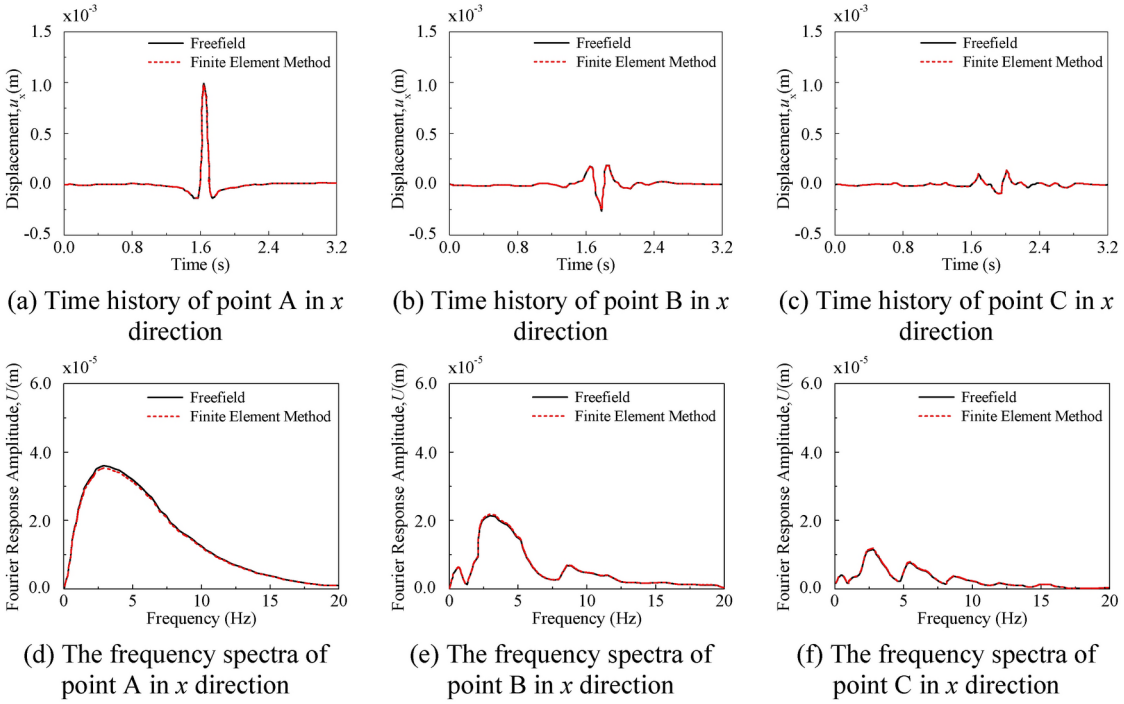

Fig. 18. The responses of each observation point in x-direction (x_1-direction).

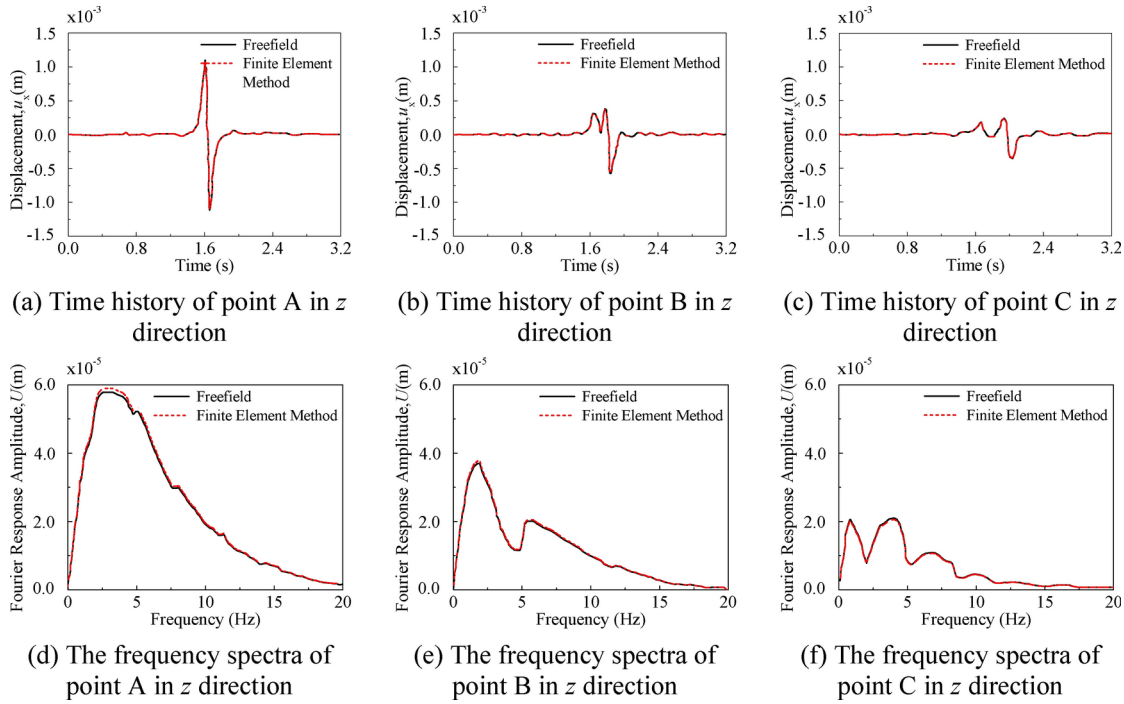

Fig. 19. The responses of each observation point in z-direction (x_2-direction).

After normalizing the calculated mode shapes at each frequency point, the first three orders of modes at 10 Hz were visualized in Fig. 17. Within the soil layers, clear turning points in the mode pattern were observed at layer intersections. At the free surface, the fundamental mode dominates, with the shortest wavelength at a given frequency due to its lowest phase velocity. As depth increases, the fundamental mode decays at a faster rate, with the proportion of other modes increasing. Higher order modes require greater depth to bring mass motion to zero.

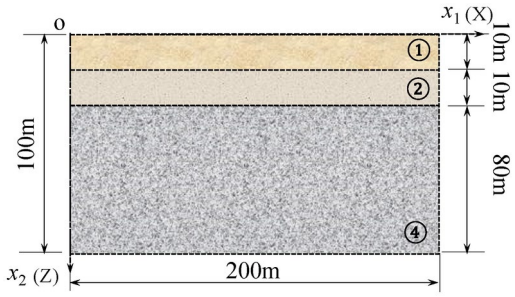

Fig. 20. Schematic diagram of the soil model for a three-layered soil site.

Material number	Soil layer thickness	Density (kg/m^3)	Modulus of elasticity (Pa)	Poisson's ratio (μ)	Rayleigh wave velocity (m/s)	Shear wave velocity (m/s)	Compression velocity (m/s)
①	10 m	800	1.0×10^8	0.25	206	224	400
②	10 m	1000	2.0×10^8	0.24	368	400	700
④	80 m	1200	6.0×10^8	0.23	413	451	760

Table 3. Parameters of the model.

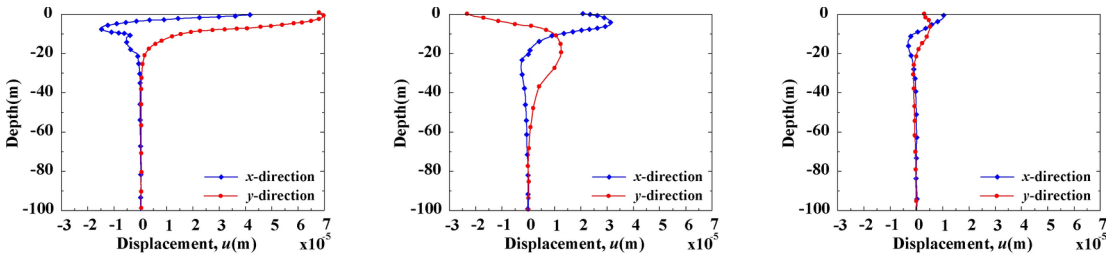

Fig. 21. Modes at 10 Hz. (Multi-layer soil site).

Employing a self-programmed FORTRAN code, we obtained the Rayleigh wave field by combining each mode at each frequency with its corresponding phase velocity. The first ten order modes were considered at each frequency point, with the cutoff frequency set to 60 Hz. Since each mode propagates independently at its corresponding phase velocity and retains its waveform during propagation, we superimposed the wavefield of each mode corresponding to each frequency point to obtain the entire Rayleigh wavefield. The wavefield boundary was then utilized as the free field input, and the wavefield response was obtained via finite element analysis. To verify the accuracy of our approach, we selected three reference points, namely A (0,0), B (50,50), and C (100,100), for comparison. As illustrated in Figs. 18 and 19, the results are highly consistent, indicating the correctness of our procedure.

Multi-layer soil wave field analysis

To validate the program's suitability for wavefield calculations in multiple soil types, we selected a 2D soil calculation area, as depicted in Fig. 20. This area consists of three layers: a 10 m deep soil layer ①, a 10 m deep soil layer ②, and an 80 m deep half-space soil layer ④. The dimensions of the 2D soil model were set to 200 m × 100 m, and the media parameters for each layer are presented in Table 3. The soil was discretized into quadrilateral four-node elements with dimensions of 1.0 m × 1.0 m in the x- and z-directions, resulting in a total of 15,000 elements and 15,651 nodes. For this example, we employed the input pulses illustrated in Fig. 3.

As illustrated in Fig. 21, the characteristics of each vibration pattern are consistent with those described in the previous section. The resulting wavefield was utilized as a free field input to obtain site response via finite element analysis. The results for the three points at coordinates (0,0), (50,50), and (100,100) are shown in Figs. 22 and 23, and they demonstrate the applicability of this procedure to Rayleigh waves in multi-layered soils. Consequently, our adopted procedure is deemed suitable for solving Rayleigh wave fields in multi-layered soils.

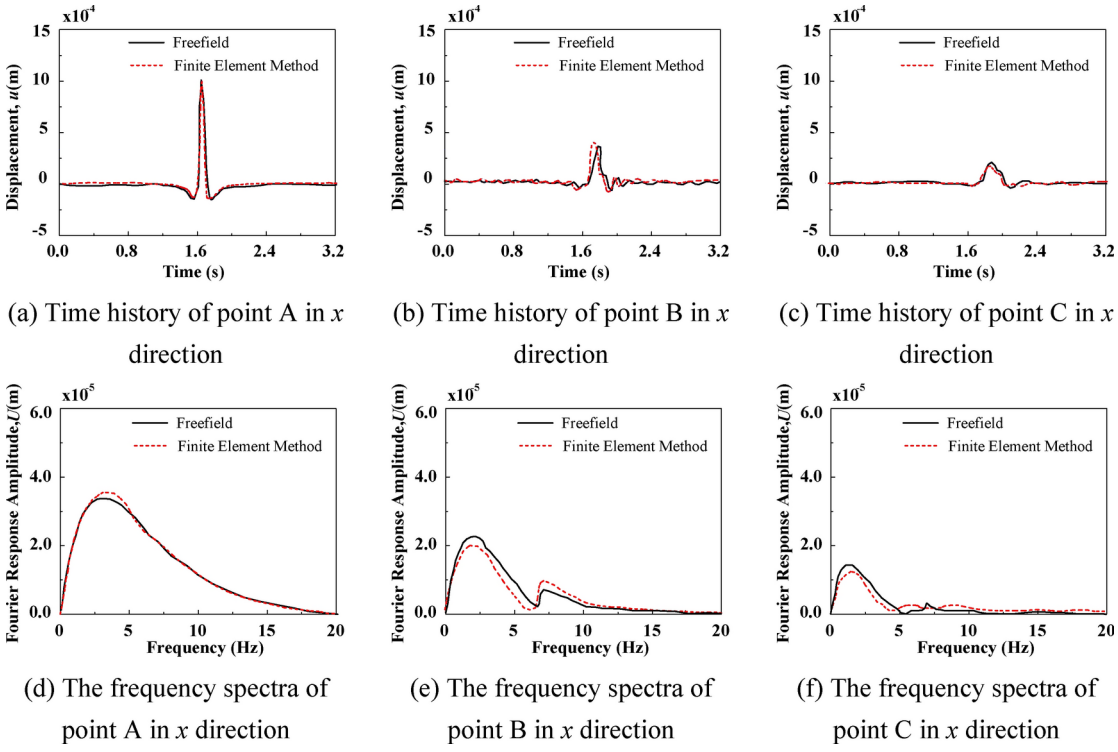

(a) Time history of point A in x direction (b) Time history of point B in x direction (c) Time history of point C in x direction

(d) The frequency spectra of point A in x direction (e) The frequency spectra of point B in x direction (f) The frequency spectra of point C in x direction

Fig. 22. The response of each observation point in x-direction (x_1-direction). (Multi-layer soil site).

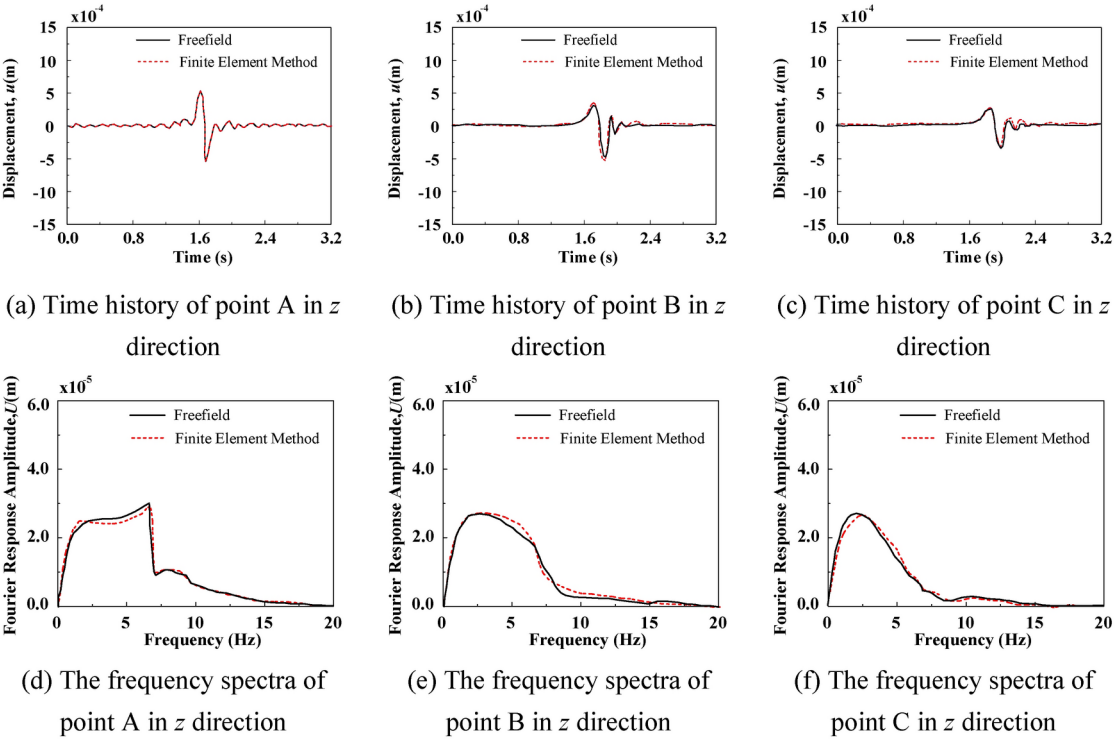

(a) Time history of point A in z direction (b) Time history of point B in z direction (c) Time history of point C in z direction

(d) The frequency spectra of point A in z direction (e) The frequency spectra of point B in z direction (f) The frequency spectra of point C in z direction

Fig. 23. The response of each observation point in z-direction (x_2-direction). (Multi-layer soil site).

The implementation of Rayleigh wavefield in stratified ground

Below is a simplified example of FORTRAN code used to synthesize the dynamic response of Rayleigh wavefield in stratified ground. Please note, this is a basic example:

```
FORTRAN
PROGRAM Rayleigh_Wave_Synthesis
  IMPLICIT NONE

  ! Type and Declarations

  INTEGER :: i, j, k, n
  REAL :: dt, t, t_max, f, omega, kx, kz, c, h
  REAL, PARAMETER :: pi = 3.1415926

  ! Parameter Setting

  n = 1000                    ! Time Steps
  t_max = 10.0                ! Maximum Simulation Time
  dt = t_max / REAL(n)        ! Time Step Length

  ! Stratified Ground Parameters

  REAL, DIMENSION(3) :: h_layer = [10.0, 20.0, 30.0]    ! Layer Depth
  REAL, DIMENSION(3) :: vp_layer = [2000.0, 2500.0, 3000.0]    ! Layer Wave Velocity
  REAL, DIMENSION(3) :: vs_layer = [1000.0, 1250.0, 1500.0]    ! Layer Shear Wave Velocity

  ! Output Rayleigh Wavefield

  OPEN(10, FILE='Rayleigh_Wave_Field.txt')

  ! Time Loop

  DO i = 1, n
    t = REAL(i) * dt

    ! Spatial Loop

    DO j = 1, 100
      kx = 2.0 * pi * REAL(j) / 100.0
      omega = 2.0 * pi / t_max

    ! Rayleigh Wave Velocity in Stratified Ground

      c = 0.0
      DO k = 1, SIZE(h_layer)
        IF (h <= h_layer(k)) THEN
          c = SQRT((omega ** 2 * (vp_layer(k) ** 2 - vs_layer(k) ** 2)) / (vp_layer(k) ** 2 + 2.0 * vs_layer(k)
** 2))
          EXIT
        END IF
      END DO

    ! Synthesis of Rayleigh Wavefield

      WRITE(10, *) t, kx, c
    END DO
  END DO

    CLOSE(10)

  END PROGRAM Rayleigh_Wave_Synthesis
```

The aforementioned FORTRAN program is utilized for synthesizing Rayleigh wavefield in stratified ground. The program computes Rayleigh wave velocity based on provided stratified ground parameters and iterates over both spatial and temporal domains to synthesize the dynamic response of Rayleigh wavefield. Ultimately, the Rayleigh wavefield data is outputted to a text file for further analysis. Practical applications may necessitate additional algorithms and input parameters to accurately simulate seismic scenarios.

Conclusions

In this study, we have developed and validated novel numerical algorithms for synthesizing Rayleigh wave fields in both uniform elastic half-spaces and horizontally layered elastic half-spaces. Our key findings and contributions are summarized as follows:

(1) We have successfully developed a FORTRAN program for synthesizing Rayleigh wave fields in a uniform elastic half-space for synthesizing Rayleigh wave fields in horizontally layered elastic half-spaces. The accuracy and effectiveness of these algorithms have been rigorously validated through comparisons with analytical solutions and benchmark problems from the literature.
(2) The relevant results indicate that: the Rayleigh waves exhibit elliptical particle motion at the free surface, transitioning from clockwise to counterclockwise motion with increasing depth. The vertical and horizontal components of Rayleigh waves decay with depth, with the horizontal component decaying more rapidly. Rayleigh wave energy is predominantly concentrated near the surface, with faster decay in the horizontal direction. Higher frequency components of Rayleigh waves decay faster with depth due to their shorter wavelengths and higher sensitivity to subsurface properties.
(3) Our study enabled the synthesis of Rayleigh wave fields for both uniform elastic half-spaces and horizontal laminated elastic half-spaces, laying the foundation for calculating soil-structure interaction with Rayleigh wave input. By extending the application of PASSI to analyze soil-structure interaction under Rayleigh wave action, our study further improved the PASSI method.

This work establishes a precedent for subsequent inquiries into the utilization of Rayleigh waves for soil-structure interaction analysis. Potential avenues for future research include the extension of these algorithms to address three-dimensional configurations and the integration of soil nonlinearity effects into the PASSI framework.

Data availability

Data is provided within the manuscript or used during the study are available from the corresponding author by request.

Received: 18 May 2024; Accepted: 19 September 2024
Published online: 28 September 2024

References

1. Lin, C.-P. & Chang, T.-S. Multi-station analysis of surface wave dispersion. *Soil Dyn. Earthq. Eng.* **24**(11), 877–886. https://doi.org/10.1016/j.soildyn.2003.11.011 (2004).
2. Socco, L. V., Foti, S. & Boiero, D. Surface-wave analysis for building near-surface velocity models-established approaches and new perspectives. *Geophysics* **75**(5), 83–102. https://doi.org/10.1190/1.3479491 (2010).
3. Dal Moro, G. *Surface Wave Analysis for Near Surface Applications* 43–64 (Elsevier Inc., 2015).
4. Rayleigh, L. On waves propagated along the plane surface of an elastic solid. *Proc. Lond. Math. Soc.* **1**, 4–11. https://doi.org/10.1112/plms/s1-17.1.4 (1885).
5. Miniaci, M., Krushynska, A., Bosia, F. & Pugno, N. M. Largescale mechanical metamaterials as seismic shields. *N. J. Phys.* **18**, 083041. https://doi.org/10.1088/1367-2630/18/8/083041 (2016).
6. Ding, W., Chen, C. & Nie, T. Analysis of Rayleigh wave dynamic response and propagation characteristics in layered media. *Value Eng.* **38**(27), 178–182 (2019) (**in Chinese**).
7. Jusoh, S. N., Mohamad, H. & Marto, A. Segment's joint in precast tunnel lining design. *J. Teknol.* **77**, 91–98. https://doi.org/10.11113/JT.V77.6426 (2015).
8. Al-Bared, M. A. *et al.* Cyclic behavior of RT-cement treated marine clay subjected to low and high loading frequencies. *Geomech. Eng.* **21**, 433–445. https://doi.org/10.12989/GAE.2020.21.5.433 (2020).
9. Chaiyasarn, K. *et al.* Integrated pixel-level CNN-FCN crack detection via photogrammetric 3D texture mapping of concrete structures. *Autom. Constr.* **140**, 104388. https://doi.org/10.1016/j.autcon.2022.104388 (2022).
10. Pan, Y. *et al.* Estimating S-wave velocities from 3D 9-component shallow seismic data using local Rayleigh-wave dispersion curves—A field study. *J. Appl. Geophys.* **159**, 532–539. https://doi.org/10.1016/j.jappgeo.2018.09.037 (2018).
11. Mi, B. *et al.* Near-surface imaging from traffic-induced surface waves with dense linear arrays: An application in the urban area of Hangzhou, China. *Geophysics* **87**, 145–158. https://doi.org/10.1190/geo2021-0184.1 (2022).
12. Yuan, D. & Nazarian, S. Automated surface wave method: Inversion technique. *J. Geotech. Eng.* **119**, 1112–1126. https://doi.org/10.1061/(ASCE)0733-9410(1993)119:7(1112) (1993).
13. Wang, H. *et al.* Understanding of seismic exploration and viewpoint of seismic data imaging processing in a complex surface exploration area. *Geophys. Prospect. Pet.* **62**, 789–805 (2023).
14. Xia, J., Miller, R. D. & Park, C. B. Estimation of near-surface shear-wave velocity by inversion of Rayleigh waves. *Geophysics* **64**, 691–700. https://doi.org/10.1190/1.1444578 (1999).
15. Yuan, S. *et al.* Finite-difference modeling and characteristics analysis of Rayleigh waves in anisotropic-viscoelastic media. *Soil Dyn. Earthq. Eng.* **108**, 46–57. https://doi.org/10.1016/j.soildyn.2018.02.004 (2018).
16. Xia, J., Xu, Y., Miller, R. D. & Ivanov, J. Estimation of near-surface quality factors by constrained inversion of Rayleigh-wave attenuation coefficients. *J. Appl. Geophys.* **82**(4), 137–144. https://doi.org/10.1016/j.jappgeo.2012.03.003 (2012).
17. Carcione, J. M. Rayleigh waves in isotropic viscoelastic media. *Geophys. J. Int.* **108**(2), 453–464. https://doi.org/10.1111/j.1365-246X.1992.tb04628.x (1992).
18. Zhang, K., Luo, Y., Xia, J. & Chen, C. Pseudospectral modeling and dispersion analysis of Rayleigh waves in viscoelastic media. *Soil Dyn. Earthq. Eng.* **31**, 1332–1337. https://doi.org/10.1016/j.soildyn.2011.05.004 (2011).
19. Todorovska, M. I. & Lee, V. W. A note on response of shallow circular valleys to Rayleigh waves: Analytical approach. *Earthq. Eng. Eng. Vib.* **10**(1), 21–34 (1990).
20. Drake, L. A. & Mal, A. K. Love and Rayleigh waves in the San Fernando valley. *Bull. Seismol. Soc. Am.* **62**(6), 1673–1690. https://doi.org/10.1785/BSSA0620061673 (1972).
21. Frankel, A. & Vidale, J. A three-dimensional simulation of seismic waves in the Santa Clara valley, California, from a Loma Prieta aftershock. *Bull. Seismol. Soc. Am.* **82**(5), 2045–2074. https://doi.org/10.1111/j.1752-4571.2011.00198.x (1992).
22. Sanchez-Sesma, F. J., Ramos-Martinez, J. & Campillo, M. An indirect boundary element method applied to simulate the seismic response of alluvial valleys for incident P, S and Rayleigh waves. *Earthq. Eng. Struct. Dyn.* **22**(4), 279–295. https://doi.org/10.1002/eqe.4290220402 (1993).
23. Kawase, H. & Aki, K. A study on the response of a soft basin for incident S, P, and Rayleigh waves with special reference to the long duration observed in Mexico City. *Bull. Seismol. Soc. Am.* **79**(5), 1361–1382 (1989).
24. Khair, K. R., Datta, S. K. & Shah, A. H. Amplification of obliquely incident seismic waves by cylindrical alluvial valley of arbitrary cross-sectional shape. Part II. Incident SH and Rayleigh waves. *Bull. Seismol. Soc. Am.* **81**(2), 346–357 (1991).
25. Currie, P. K., Hayes, M. A. & O'Leary, P. M. Viscoelastic Rayleigh waves. *Q. Appl. Math.* **35**, 35–53 (1977).
26. Carcione, J. M. Modeling anelastic singular surface waves in the Earth. *Geophysics* **57**(6), 781–792. https://doi.org/10.1190/1.1443292 (1992).
27. Lan, H. & Zhang, Z. Comparative study of the free-surface boundary condition in two-dimensional finite-difference elastic wave field simulation. *J. Geophys. Eng.* **8**, 275–286 (2011).
28. Xu, Y., Xia, J. & Miller, R. D. Numerical investigation of implementation of air-earth boundary by acoustic-elastic boundary approach. *Geophysics* **72**, 147–153 (2007).
29. Bohlen, T. & Saenger, E. H. Accuracy of heterogeneous staggered-grid finite-difference modeling of Rayleigh waves. *Geophysics* **71**, 109–115 (2006).
30. Gottschammer, E. & Olsen, K. B. Accuracy of the explicit planar free-surface boundary condition implemented in a fourth-order staggered-grid velocity-stress finite-difference scheme. *Bull. Seismol. Soc. Am.* **91**, 617–623 (2001).
31. Kristek, J., Moczo, P. & Archuleta, R. J. Efficient methods to simulate planar free surface in the 3D 4th-order staggered-grid finite-difference schemes. *Stud. Geophys. Geod.* **46**, 355–381 (2002).
32. Fang, X., Yao, G., Niu, F. & Wu, D. Estimating optimal parameters of finite-difference scheme for wavefield modeling. *Chin. J. Geophys.* **66**, 2520–2533 (2023).
33. Yao, G., Wu, D. & Debens, H. A. Adaptive finite difference for seismic wavefield modelling in acoustic media. *Sci. Rep.* **6**, 30302. https://doi.org/10.1038/srep30302 (2016).
34. Dutta, G. & Schuster, G. T. Attenuation compensation for least-squares reverse time migration using the viscoacoustic-wave equation. *Geophysics* **79**, S251–S262 (2014).

35. Borcherdt, R. D. Rayleigh-type surface wave on a linear viscoelastic half-space. *J. Acoust. Soc. Am.* **54**, 1651–1653 (1973).
36. Yuan, S., Song, X., Cai, W. & Hu, Y. Analysis of attenuation and dispersion of Rayleigh waves in viscoelastic media by finite difference modeling. *J. Appl. Geophys.* **148**, 115–126 (2018).
37. Carcione, J. M., Kosloff, D. & Kosloff, R. Wave propagation simulation in a linear viscoelastic medium. *Geophys. J. Int.* **95**, 597–611 (1988).
38. Xu, T. & McMechan, G. A. Composite memory variables for viscoelastic synthetic seismograms. *Geophys. J. Int.* **121**, 634–639 (1995).
39. Savage, B., Komatitsch, D. & Tromp, J. Effects of 3D attenuation on seismic wave amplitude and phase measurements. *Bull. Seismol. Soc. Am.* **100**, 1241–1251 (2010).
40. Zhu, T., Carcione, J. M. & Harris, J. M. Approximating constant-Q seismic propagation in the time domain. *Geophys. Prospect.* **61**, 931–940 (2013).
41. Wang, N. *et al.* Fractional Laplacians viscoacoustic wavefield modeling with k-space based time-stepping error compensating scheme. *Geophysics* **85**, T1–T13 (2020).
42. Wang, N. *et al.* Propagating seismic waves in VTI attenuating media using fractional viscoelastic wave equation. *J. Geophys. Res. Solid Earth.* **127**, e2021JB023280 (2022).
43. Carcione, J. M., Cavallini, F., Mainardi, F. & Hanyga, A. Time-domain modeling of constant-Q seismic waves using fractional derivatives. *Pure Appl. Geophys.* **159**, 1719–1736 (2002).
44. Carcione, J. M. Theory and modeling of constant-Q P-and S-waves using fractional time derivatives. *Geophysics* **74**, T1–T11 (2009).
45. Lysmer, J. Lumped mass method for Rayleigh waves. *Bull. Seismol. Soc. Am.* **60**(1), 89–104 (1970).
46. Waas, G. Linear two-dimensional analysis of soil dynamics problems in semi-infinite layered media. The University of California (1972).
47. Kausel, E. & Peek, R. Dynamic loads in the interior of a layered stratum: An explicit solution. *Bull. Seismol. Soc. Am.* **72**(5), 1459–1481 (1982).
48. Chen, S. L., Lv, H. & Zhou, G. L. Partitioned analysis of soil structure interaction for nuclear island building. *Earthq. Eng. Struct. D.* **51**, 2220–2247. https://doi.org/10.1002/eqe.3661 (2022).
49. Lv, H. & Chen, S. Analysis of nonlinear soil structure interaction using Partitioned method. *Soil Dyn. Earthq. Eng.* **162**, 107470. https://doi.org/10.1016/j.soildyn2022.107470 (2022).
50. Lv, H. & Chen, S. Seismic response characteristics of nuclear island structure at generic soil and rock sites. *Earthq. Eng. Eng. Vib.* **22**, 667–688. https://doi.org/10.1007/s11803-023-2186-8 (2023).
51. Liao, Z. P., Yang, B. P. & Yuan, Y. F. Artificial boundary in analysis of transient elastic wave propagation. *Earthq. Eng. Eng. Vib.* **2**(1), 1–11 (1982).
52. Liao, Z. P. & Wong, H. A transmitting boundary for the numerical simulation of elastic wave propagation. *Int. J. Soil Dyn. Earthq. Eng.* **3**, 174–183. https://doi.org/10.1016/0261-7277(84)90033-0 (1984).
53. Liao, Z. P. Dynamic interaction of natural and man-made structures with earth medium. *Earthq. Res. China* **3**, 367–408 (1999).
54. Wang, Y. Frequencies of the Ricker wavelet. *Geophysics* **80**, A31–A37. https://doi.org/10.1190/geo2014-0441.1 (2015).
55. Zhang, K. *et al.* Analysis on the cross of Rayleigh-wave dispersion curves in viscoelastic layered media. *Chin. J. Geophys.* **59**(3), 972–980 (2016).
56. Qin, B., Cao, Y. M. & Xia, H. Comparison of two calculation methods of Rayleigh waves dispersion curve. *J. Hebei Univ. Eng. (Nat. Sci. Ed.)* **28**(2), 10–13 (2011) (**in Chinese**).

Acknowledgements

I would like to express my sincere gratitude to my PhD supervisor, Prof Shaolin Chen, for sharing their methodology and experience with me and making this work possible. The authors gratefully acknowledge the financial support of this work by the Postdoctoral Fellowship Program of CPSF under Grant Number: GZC20231496, and the Shandong Postdoctoral Science Foundation (No. SDCX-ZG-202400217).

Author contributions

Data curation: H.L.; Methodology: H.L.; Resources: H.L.; Software: H.L.; Supervision: H.L.; Validation: H.L.; Visualization: H.L.; Writing—original draft: H.L.

Competing interests

The authors declare no competing interests.

Additional information

Correspondence and requests for materials should be addressed to H.L.